Magnetism and spin transport in rare-earth-rich epitaxial terbium and europium iron garnet films

Ethan R. Rosenberg,[1] Lukáš Beran,[1,2] Can O. Avci,[1] Cyrus Zeledon,[1,3] Bingqian Song,[1] Claudio Gonzalez-Fuentes,[4] Johannes Mendil,[5] Pietro Gambardella,[5] Martin Veis,[2] Carlos Garcia,[4] Geoffrey S. D. Beach,[1] and Caroline A. Ross[1]

[1]*Department of Materials Science and Engineering, Massachusetts Institute of Technology, Cambridge, Massachusetts 02139, USA*
[2]*Faculty of Mathematics and Physics, Charles University, Ke Karlovu 3, 12116 Prague 2, Czech Republic*
[3]*Department of Materials Science and Engineering, Cornell University, Ithaca, New York 14850, USA*
[4]*Departament of Physics, Universidad Técnica Federico Santa María, Avenida España 1680, 2390123 Valparaíso, Chile*
[5]*Department of Materials, ETH Zürich, CH-8093 Zürich, Switzerland*

Rare-earth iron garnet thin films with perpendicular magnetic anisotropy (PMA) have recently attracted a great deal of attention for spintronic applications. Thulium iron garnet (TmIG) has been successfully grown and TmIG/Pt heterostructures have been characterized. However, TmIG is not the only rare-earth iron garnet that can be grown with PMA. We report the growth, magnetic, and spintronic properties of epitaxial terbium iron garnet (TbIG) and europium iron garnet (EuIG) thin films with PMA. Reciprocal space mapping shows the films are lattice matched to the substrate without strain relaxation, even for films up to 56 nm thick. The lattice strain and magnetostriction coefficient produce PMA in certain cases. TbIG grows on (111) gadolinium gallium garnet (GGG) with PMA due to the in-plane compressive strain, whereas TbIG on (111) substituted GGG (SGGG) is in tension and has an in-plane easy axis. EuIG grows with PMA on (100) and (111) GGG substrates, which facilitates the investigation of spintronic properties as a function of orientation. Both garnets have excess rare earth, which is believed to occupy Fe octahedral sites and in the case of TbIG is associated with an increase in the compensation temperature to 330 K, higher than the bulk value. Anomalous Hall effect (AHE) measurements of Pt/EuIG Hall crosses show that the spin mixing conductance of Pt/ (111) and (100) EuIG is similar. AHE measurements of Pt/TbIG Hall crosses reveal a sign change in the AHE amplitude at the compensation point analogous to all-metallic systems.

I. INTRODUCTION

Spin transport across heavy metal/ferrimagnetic insulator (HM/FMI) interfaces has attracted a great deal of interest over the past decade. Magnon-mediated spin currents in $Y_3Fe_5O_{12}$ (YIG) were observed by the inverse spin Hall effect in a Pt overlayer [1,2], and conversely a spin-orbit torque (SOT) produced by the Pt layer was used for the propagation and subsequent detection of magnons in YIG [1,3]. These results suggested the possible manipulation of the magnetization of insulating materials with an electric current. SOT-assisted reversal was reported in barium hexaferrite [4], but the first reported switching of a HM/FMI structure by SOT utilized $Tm_3Fe_5O_{12}$ (TmIG or thulium iron garnet) as the FMI layer [5]. Electrical switching of magnetization has applications in SOT-magnetic random access memory and other emerging memory technologies. Materials with perpendicular magnetic anisotropy (PMA) are desirable for such devices because they allow for higher bit densities [6,7]. There has been extensive work on SOT switching of PMA ferromagnetic metals such as Co and CoFeB [8–11], but FMIs have two advantages over metals: a more favorable scaling behavior, because the PMA originates from bulk rather than interface anisotropy; and prevention of current shunting from the SOT-producing HM layer [4].

The best studied FMI is YIG, which is a good insulator with exceptionally low damping, as well as a low

magnetostriction and magnetocrystalline anisotropy. YIG films typically exhibit an in-plane easy axis dominated by shape anisotropy, although there are reports of thin YIG films showing PMA [12–14]. Other FMI films have been grown with PMA, notably barium hexaferrite ($BaFe_{12}O_{19}$, BaM) grown epitaxially on sapphire with anisotropy field of 17 kOe [4,15]; and Co ferrite ($CoFe_2O_4$) grown epitaxially on substrates such as $SrTiO_3$ or MgO [16,17]. Rare-earth iron garnets (REIG) with PMA have also been developed, in which the PMA originates from magnetoelastic anisotropy due to the epitaxial mismatch strain of the REIG on the gadolinium iron garnet (GGG) substrate [12,18]. TmIG [5,18,19], SmIG ($Sm_3Fe_5O_{12}$) [20], and TbIG ($Tb_3Fe_5O_{12}$) [21] films, as well as Ce- or Bi-substituted YIG [22–24], exhibit strain-induced PMA. Other thin film RE garnets include GdIG ($Gd_3Fe_5O_{12}$) [25] and LuIG ($Lu_3Fe_5O_{12}$) [26] with in plane easy axis. Out of the PMA RE garnets, TmIG is the most extensively studied in terms of the spintronic properties of the FMI/HM interface [19,27–30]. TmIG/HM devices exhibited SOT-driven reversal with applied fields as low as 2 Oe and evidence of fast current-induced domain wall velocities reaching 1000 m/s at a current density of 2.5×10^{12} A/m^2 in the Pt [28]. TmIG/Pt heterostructures were also recently used to study the validity of the bulk spin Hall effect model for SOT [29].

In this paper, we describe the growth, structure, and the magnetic and spintronic properties of two rare-earth iron garnets: TbIG and EuIG ($Eu_3Fe_5O_{12}$). These materials were
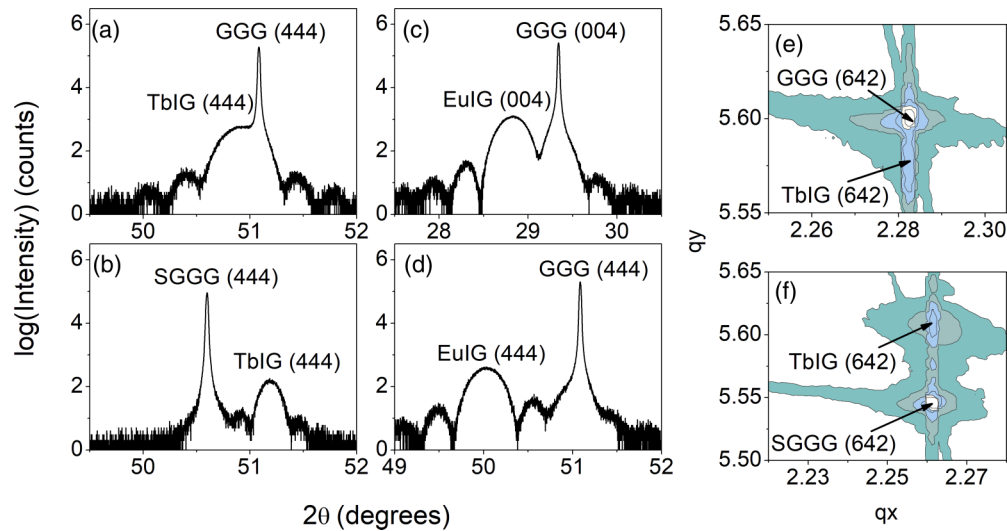
FIG. 1. [(a)–(d)] High-resolution XRD ω-2θ scans of representative EuIG and TbIG thin films [(e) and (f)] High-resolution XRD reciprocal space maps of TbIG/GGG and TbIG/SGGG thin films.

selected based on their bulk magnetostriction values and their lattice mismatch with respect to GGG, which lead to a magnetoelastic anisotropy contribution that determines the net anisotropy of the film [31,32]. For TbIG and TmIG, the two magnetostriction coefficients λ_{111} and λ_{100} have opposite sign and PMA is expected in films grown epitaxially on (111) GGG but not on (001) GGG [31]. In contrast, the two magnetostriction coefficients of EuIG are of the same sign and EuIG/GGG is expected to exhibit PMA in both the (111) and (001) orientations. EuIG and TbIG were grown by pulsed laser deposition and the composition is enriched in RE compared with the target. We demonstrate efficient spin transport through Pt/TbIG and Pt/EuIG interfaces through anomalous Hall effect-like spin Hall magnetoresistance (AHE-like SMR) measurements and show that the spin-mixing conductance of Pt/EuIG is approximately orientation-independent, in contrast to what has been observed in Pt/cobalt ferrite heterostructures [16]. We demonstrate by magnetometry, magnetoresistance, and optical measurements the presence of a compensation temperature [31] near room temperature in TbIG, and report the damping coefficient of the EuIG (111) films.

II. STRUCTURAL AND MAGNETIC CHARACTERIZATION

EuIG and TbIG thin films of thicknesses varying from 10 to 90 nm were grown on GGG (lattice parameter $a = 1.2376$ Å) and substituted GGG (SGGG, $a = 1.2497$ Å) using pulsed laser deposition (PLD) in an oxygen pressure of 150 mTorr. In all cases, the substrate was placed on a sample holder heated to a backside temperature of $900\,^\circ$C. The frontside (substrate) temperature was not measured directly but was ~$250\,^\circ$C lower. The targets used in these depositions were prepared by sintering [19]. Further information on the film and target preparation is presented in the Methods section.

The high crystalline quality of these films is evident from the Laue fringes present in each symmetric (444) scan in Figs. 1(a)–1(d), which were taken from representative thin films of each type. Figures 1(e) and 1(f) show reciprocal space maps of the (642) reflection of 52 nm thick TbIG

films grown on GGG and SGGG substrates. In both cases, the substrate peak is vertically aligned with the film peak, indicating that the films are fully strained to the substrate. This pseudomorphic growth was seen in all of the films prepared for this study and for TbIG films up to 90 nm in thickness.

Compositional analysis was carried using x-ray photoelectron spectroscopy (XPS) for representative TbIG/GGG and EuIG/GGG (001) samples (Fig. 2). The RE:Fe ratio exceeds 0.6 in both cases, with values of 0.72 for EuIG (001) and 0.70 for TbIG. This iron deficiency is consistent with similar XPS analyses of sputtered TmIG films and PLD-grown YIG films, which showed Y:Fe ratios as large as 1.37 [27,33].

The XRD did not indicate any nongarnet peaks suggesting that the excess RE is incorporated into the garnet lattice. Although the RE ions have a larger ionic radius than the Fe^{3+}, RE ions including Eu^{3+} and Eu^{2+} can be present within octahedral sites of oxides such as $BaTiO_3$ [34]. Tb^{3+}, on the other hand, transitions to Tb^{4+} (a stable $4f^7$ ion) in order to enter octahedral sites [35]. Indeed, the high resolution XPS spectra (Fig. 3) indicate the presence of Tb^{3+}, Tb^{4+}, Eu^{3+}, and Eu^{2+} in our films [36,37]. Considering the smaller size of the tetrahedral site, we assume that the RE ions preferentially occupy the octahedral sites. The ability for the RE ions to enter octahedral sites can explain why the garnets are able to crystallize even when the RE:Fe ratio substantially exceeds 0.6. The presence of octahedral RE ions has profound implications for the sublattice magnetization and compensation temperature since the magnetic moment of the RE ions differs from that of the Fe^{3+} which they replace. Furthermore, in order to maintain charge neutrality when the RE valence state differs from +3, Fe^{2+} or Fe^{4+} ions as well as oxygen vacancies may be present in the films. The valence states of the Fe could not be resolved in the XPS data.

The magnetic properties of the thin films were characterized using vibrating sample magnetometry (VSM). Easy- and hard-axis hysteresis loops for representative TbIG and EuIG films are displayed in Fig. 3. The net anisotropy of the films is determined by the magnetocrystalline, shape, and magnetoelastic anisotropy contributions. The magnetocrystalline
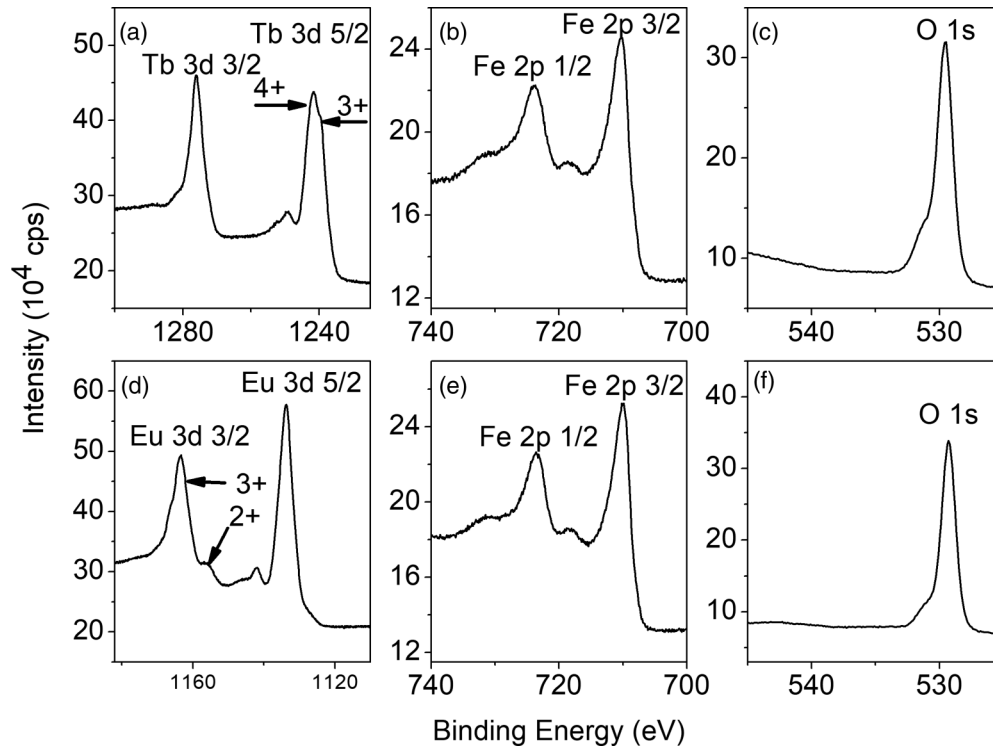
FIG. 2. (Tb,Eu) $3d$, Fe $2p$, and O $1s$ spectra of representative TbIG and EuIG thin films. In the RE spectra, peaks belonging to each oxidation state are marked.

anisotropy K_1 is small but negative, and favors PMA for (111) films, whereas the shape anisotropy favors an in-plane magnetization. The PMA is primarily driven by magnetoelastic anisotropy overcoming the shape anisotropy. We write the uniaxial anisotropy K_u as the difference between the magnetic energy for magnetization oriented in-plane and the energy for magnetization oriented out-of-plane, where the three terms on the right represent the magnetocrystalline, magnetoelastic, and shape anisotropies:

$$K_u = E_{IP} - E_{OP}$$
$$= -\frac{K_1}{12} - \frac{9}{8}\lambda_{111}c_{44}\left(\frac{\pi}{2} - \beta\right) + \left(\frac{\mu_0}{2}\right)M_s^2, \quad (1)$$

where λ_{111} is the relevant magnetostriction coefficient for the (111) films, c_{44} is the shear modulus, β is the corner angle of the rhombohedrally-distorted unit cell, and M_s is the saturation magnetization [19,38,39].

From this equation and from the list of bulk garnet properties in Table I [31], we expect PMA (i.e., a negative K_u) in (111) TbIG under sufficient in-plane compressive strain. The dominant effect of the magnetoelastic contribution is illustrated by a comparison of the net anisotropy of (111) TbIG/GGG and TbIG/SGGG films. Based on the bulk lattice parameters of TbIG, GGG, and SGGG, we expect an epitaxial TbIG film to be under in-plane compression on GGG and in-plane tension on SGGG, which is verified by the x-ray data in Fig. 1. The VSM hysteresis loops in Fig. 3 indeed show an out-of-plane square loop for TbIG/GGG(111) [Fig. 3(a); compressive strain], while the TbIG/SGGG(111) sample [Fig. 3(b); tensile strain] shows a square in-plane

hysteresis loop. Hard-axis loops for TbIG are not shown because the saturation field is higher than the maximum field of 10 kOe available in the VSM. We attempted to ascertain the anisotropy field in a SQUID magnetometer at higher fields, but the large paramagnetic signal from the GGG substrate made it difficult to determine when the TbIG films were saturated.

A similar calculation for EuIG films indicates that compressively strained films on both (001) and (111) GGG are expected to show PMA. This is verified by the in- and out-of-plane VSM hysteresis loops in Figs. 3(c) and 3(f), together with the coupled XRD scans in Figs. 1(c) and 1(d). PMA is retained up to 56-nm thickness, which is consistent with the x-ray data showing little or no strain relaxation. The saturation magnetization, whose measured values range from 110–118 emu cm^{-3}, is higher than the bulk value of 93 emu cm^{-3} [31], which may be a result of the excess Eu. For both the (111) and the (001) films, the coercivity increased with increasing thickness. The anisotropy field was determined from the hard-axis loops by fitting a straight line to the $M(H)$ curve near zero field and extrapolating to the saturation magnetization. The saturation magnetization was obtained from the easy axis hysteresis loops.

By measuring the strain state from the x-ray data and the anisotropy field from VSM, the thin-film values of λ_{111} and λ_{100} may be found. For the (111) case, a cubic unit cell distorted along one of its [111] directions becomes rhombohedral, and we use a rhombohedral-to-hexagonal transformation to greatly simplify the calculation of strain [40]. The transformation from rhombohedral to hexagonal Miller indices [(*hkl*)
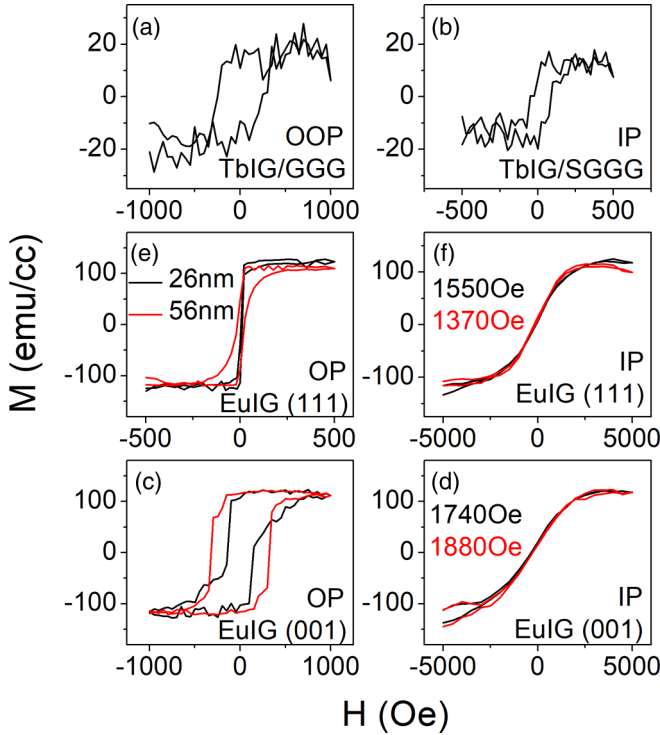
FIG. 3. In-plane (IP) and out-of-plane (OOP) VSM hysteresis loops of representative TbIG and EuIG thin films. In the IP EuIG hysteresis loops, the estimated anisotropy fields are presented and are color-coded (color online) in the same manner as the loops.

to (*HKL*)] is given by

$$\begin{pmatrix} H \\ K \\ L \end{pmatrix} = \begin{pmatrix} 1 & -1 & 0 \\ 0 & 1 & -1 \\ 1 & 1 & 1 \end{pmatrix} \begin{pmatrix} h \\ k \\ l \end{pmatrix}. \quad (2)$$

The in-plane lattice parameter of the hexagonal unit cell is given by [40]

$$a_H = \sqrt{12 d_{11\bar{2}}^2}, \quad (3)$$

where $d_{11\bar{2}}$ is the $(11\bar{2})$ plane spacing in the rhombohedral unit cell, assumed to be equal to the $(11\bar{2})$ spacing in the substrate. Finally, the corner angle of the unit cell α is given by [40]

$$\sin\left(\frac{\alpha}{2}\right) = \frac{3}{2\sqrt{3 + \left(\frac{c}{a_H}\right)^2}}, \quad (4)$$

where c is the body diagonal of the rhombohedral cell (or the c-axis lattice parameter of the hexagonal cell). The (001) case

proceeds in a simpler manner due to the preservation of the orthogonality of the unit cell axes even after strain. For the (001) films, the uniaxial magnetoelastic anisotropy is given by [38,39]

$$K_u = -\frac{3}{2}\lambda_{100}(c_{11} - c_{12})(\varepsilon_{zz} - \varepsilon_{xx}) + \frac{\mu_0}{2}M_s^2, \quad (5)$$

where ε_{ii} is the ith axial strain component.

Table I shows the values of λ_{100} and λ_{111} for the EuIG films, derived from the total anisotropy measured from the hard axis loops, compared to published bulk values of the magnetostriction parameters [31]. K_1 was neglected in the calculations as it is much smaller than the magnetoelastic and shape anisotropy terms. Also listed in Table I are the lattice strain determined from the x-ray data and the calculated and literature values [31] for unit cell volume for both EuIG and TbIG. It is interesting to note that, despite the iron deficiency, the unit cell volumes in our films are close to the bulk values.

The calculated magnetostriction in the EuIG films differed from bulk values, and for TbIG, the high anisotropy field suggests that λ_{111} of the film exceeded the bulk value. The difference in film magnetostriction compared to bulk values may be an effect of the excess RE, or of Jahn-Teller Fe ions. For example, Fe^{2+} ions in EuIG may cause an enhancement of λ_{111} [41]. However, the XPS contributions from Fe^{3+} and Fe^{2+} cannot easily be separated [42,43].

Broadband FMR measurements of EuIG/GGG (111) with thicknesses of 26 and 56 nm were carried out at frequencies of $f = 3-6$ GHz in fields up to 4.5 kOe to determine the resonance frequency H_{res} and the linewidth ΔH. H_{res} values were averaged for two perpendicular in-plane directions of H. The Gilbert damping parameter α was obtained from the slope of ΔH vs f. The data gave a linear plot in which the slope is given by $2\alpha/\gamma$, where γ is the gyromagnetic ratio. This yielded $\alpha = 25.7 \times 10^{-3}$ (4% error) for the 26-nm-thick film and $\alpha = 24.2 \times 10^{-3}$ (17% error) for the 56-nm-thick film. These values are two orders of magnitude greater than the damping of YIG films, and are attributed to the presence of RE, especially in the RE-rich films. Studies on RE-doped YIG have shown that increasing the RE concentration greatly increases the damping parameter [44,45].

III. SPINTRONIC INTERFACE PROPERTIES

In order to characterize the room-temperature spin transport properties of the HM/FMI interface, we have obtained an estimate of the spin mixing conductance of Pt/(Tb,Eu)IG heterostructures, which is an indicator of the efficiency of spin transport through the interface

TABLE I. Results of the structural and magnetic characterization of representative EuIG and TbIG films. Experimental values of H_k and λ_{111} are not listed for TbIG because it was not saturated in-plane. Errors in H_k and M_s values are ~5%.

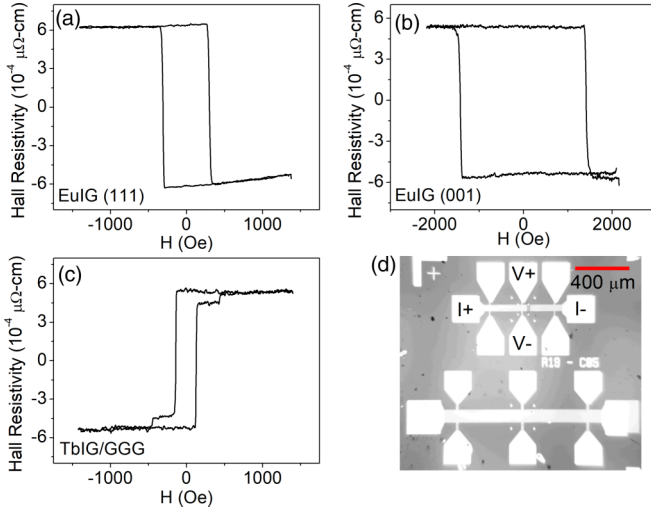| Material	β (degrees)	ε_{xx}	ε_{zz}	H_k (Oe)	M_s (300 K) (emu/cc)	$\lambda_{ijk}(10^{-6})$ (calculated)	$\lambda_{ijk}(10^{-6})$ (literature)	$V_{cell}(nm^3)$ (calculated)	$V_{cell}(nm^3)$ (literature)
EuIG/GGG (111)	89.25	n/a	n/a	1370	110	$\lambda_{111} = 14$	$\lambda_{111} = 1.8$	1.93	1.95
EuIG/GGG (001)	90	0.00796	−0.00934	1880	120	$\lambda_{100} = 5.0$	$\lambda_{100} = 21$	1.89	1.95
TbIG/GGG (111)	89.88	n/a	n/a	n/a	19	n/a	$\lambda_{111} = 12$	1.90	1.92

FIG. 4. [(a)–(c)] Anomalous-Hall-like SMR hysteresis loops for Pt(4)/REIG(10) heterostructures. (d) Optical micrograph of representative Hall crosses used for data acquisition.

[46,47]. Hall bar structures [see Fig. 4(d)] were fabricated on Pt(4 nm)/(Tb,Eu)IG(10 nm)/GGG multilayers using photolithography and ion milling techniques, and a lock-in technique [5] was used to collect anomalous Hall effect (AHE)-like spin Hall magnetoresistance (SMR) hysteresis loops. All garnet films used for Hall bar fabrication had <1 nm rms roughness as characterized by atomic force microscopy. A sample-dependent offset and a linear background due to the ordinary Hall effect (OHE) in Pt was subtracted, and the results are displayed in Figs. 4(a)–4(c). The square shape of these hysteresis loops matches the out-of-plane magnetometry data. However, the coercivity of the Hall cross is higher than that of the unpatterned film due to the effects of edge roughness on domain nucleation and pinning [5]. In-plane SMR was not measured because the probe station could not supply large enough in-plane fields to saturate the Hall cross devices.

The origin of the AHE in Pt/ferrite interfaces is a hotly debated topic, with some arguing that it is at least partly due to the magnetic proximity effect (MPE) [30,48] while others maintain that it is fully due to a spin Hall magnetoresistance (SMR) effect [5,49]. Meanwhile, measurements of the magnetic polarization of Pt in direct contact with a magnetic insulator using x-ray methods indicate that the MPE is negligibly small at room temperature [50–53]. In the following discussion, we will assume that the AHE is predominantly due to SMR, as in Avci *et al.* for the similar Pt/TmIG system [5], and consistent with the lack of MPE at room temperature in other studies [54]. The model of Chen *et al.* for spin mixing conductance [46] leads to

$$
\frac{\Delta\rho_1}{\rho} = \frac{\theta_{SH}^2 \lambda}{d_N} \frac{2\lambda G_r \tanh^2 \frac{d_N}{2\lambda}}{\sigma + 2\lambda G_r \coth \frac{d_N}{2\lambda}}
$$

$$
\frac{\Delta\rho_2}{\rho} \approx \frac{2\theta_{SH}^2 \lambda^2}{d_N} \frac{\sigma G_i \tanh^2 \frac{d_N}{2\lambda}}{\left(\sigma + 2\lambda G_r \coth \frac{d_N}{2\lambda}\right)^2},
\tag{6}
$$

TABLE II. Lower bounds of G_i for Pt/REIG heterostructures, calculated in the manner described.

Material	Lower bound of G_i
Pt/EuIG/GGG (111)	$4.6 \times 10^{12}\ \Omega^{-1}\ \mathrm{m}^{-2}$
Pt/EuIG/GGG (001)	$5.4 \times 10^{12}\ \Omega^{-1}\ \mathrm{m}^{-2}$
Pt/TbIG/GGG (111)	$4.6 \times 10^{12}\ \Omega^{-1}\ \mathrm{m}^{-2}$
Pt/TmIG/GGG (111) Ref. [5]	$7.1 \times 10^{12}\ \Omega^{-1}\ \mathrm{m}^{-2}$

where $\Delta\rho_1$ is the amplitude of an in-plane SMR loop, $\Delta\rho_2$ is the amplitude of an AHE-like SMR loop, ρ is the resistivity of the Pt layer, λ is the spin diffusion length of the Pt layer, θ_{SH} is the spin Hall angle, d_N is the Pt thickness, and $\sigma = 1/\rho$ is the Pt conductivity. G_r and G_i are the real and imaginary parts of the spin mixing conductance, respectively. While G_r can be calculated directly from a measurement of $\Delta\rho_1$, it is necessary to know G_r to calculate G_i from a measurement of $\Delta\rho_2$. Without being able to saturate the film in plane during the electrical measurement, $\Delta\rho_1$ and hence G_r could not be determined. However, previous results for similarly constructed Pt/TmIG Hall bars have values for λG_r that are an order of magnitude lower than σ ($2.07 \times 10^6\ \Omega^{-1}\ \mathrm{m}^{-1}$ for our Hall bars) [5,28]. Thus we can obtain a lower bound for G_i by dropping the G_r term in the denominator. By substituting values used in a previous study on TmIG [5] for λ and θ_{SH}, we calculate the lower bounds for G_i displayed in Table II.

These data lead to several conclusions about the spintronic properties of EuIG/Pt and TbIG/Pt heterostructures. First, even the lower bound of G_i for Pt/EuIG/GGG and Pt/TbIG/GGG is on the same order of magnitude as G_i in Pt/TmIG/GGG(111) [5], indicating a similar interfacial spin transparency in these materials. Also, G_i for Pt/EuIG/GGG(001) is almost identical to that of Pt/EuIG/GGG(111). The effect of crystal orientation on G_i at metal/ferrimagnetic insulator interfaces has received little study. However, Isasa *et al.* [16] characterized Pt/CFO by fabricating Pt Hall bars on epitaxial CFO(001)/STO and CFO(111)/STO thin films and found G_r^{111} to be significantly lower than G_r^{001}, especially in devices made using an *ex situ* process similar to ours. This observation was related to a difference in surface termination between the two orientations. A recent theoretical study by Cahaya *et al.*, which considered the effects of crystal field splitting on spin mixing conductance supports this claim [55]. A study of the orientation dependence of G_r in Pt/EuIG would provide an interesting comparison to Pt/CFO [16].

IV. TEMPERATURE-DEPENDENT PROPERTIES OF TbIG FILMS

Bulk TbIG has a magnetic compensation temperature T_{comp} of 248.6 K [31], making it a convenient system for measuring spintronic phenomena near compensation (GdIG also has a near-RT T_{comp}, but its weak magnetostriction limits its magnetoelastic anisotropy). T_{comp} of the TbIG films was measured using three different temperature-dependent techniques. The simplest of these was a temperature-dependent magnetization measurement using VSM [Fig. 5(a)], in which a minimum in
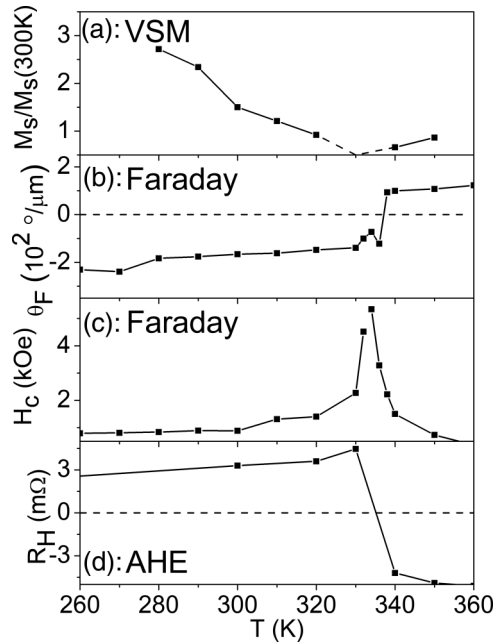
FIG. 5. Temperature-dependent measurements of (a) magnetic moment, (b) Faraday rotation, (c) coercivity, and (d) AHE-like SMR amplitude. All of these techniques agree on a magnetic compensation point of ~335 K.

the magnetic moment is clearly present near 330 K. The VSM data yield a value for T_{comp} in the range of 320 K to 340 K, indicated by a dashed line.

Temperature-dependent AHE-like SMR and Faraday rotation measurements are shown in Figs. 5(b) and 5(d). Instead of going to zero, both datasets exhibit a sign change at T_{comp} due to the reorientation of the three magnetic sublattices. Below T_{comp}, the octahedral Fe^{3+} and the Tb^{3+} moments are oriented parallel to the field and the tetrahedral Fe^{3+} moments are antiparallel, while above T_{comp} the orientation is reversed [56]. Because the Faraday effect and the SMR are sensitive to one of the magnetic sublattices rather than to the net magnetization, they exhibit a sign change at T_{comp} [56,57]. These measurements show a compensation point of around 335 K, agreeing with the VSM result in Fig. 5(a). In addition, the coercivity of the TbIG film as a function of temperature measured from the Faraday rotation hysteresis loops is depicted in Fig. 5(c). As expected for a compensated ferrimagnet, the coercivity diverges approaching the compensation point.

The T_{comp} in our TbIG thin films is higher than that of bulk TbIG by 85 K, which is attributed to the Fe deficient composition. The compensation point is determined by the difference in magnitude of the magnetic moment on the sublattices and therefore depends on the composition [57,58]. The TbIG is expected to accommodate the excess Tb as Tb^{4+} ions (magnetic moment of $7\mu_B$) on octahedral sites normally occupied by Fe^{3+} ($5\mu_B$). Fe^{2+} ions ($4\mu_B$), which have a preference for octahedral sites over tetrahedral sites as seen in the inverse spinel magnetite, may also be present. The structure can then be described as consisting of one sublattice of dodecahedral sites containing Tb^{3+} plus octahedral sites with a mixture of Fe^{3+}, Tb^{4+}, and possibly Fe^{2+}, and the other sublattice of tetrahedral sites containing Fe^{3+}. The

dodecahedral plus octahedral sublattice moment exceeds that in stoichiometric TbIG, which explains the increase in T_{comp}. This is consistent with previous measurements of the Bi:TbIG system where it was found that reducing the Tb:Fe ratio to 0.48 through the addition of Bi caused a reduction in T_{comp} to 183 K [59] because the magnetization of the dodecahedral plus octahedral sublattice was reduced with respect to that of the tetrahedral sublattice.

V. CONCLUSION

Epitaxial EuIG and TbIG thin films were grown using PLD on GGG and SGGG substrates. All films (from 10–60-nm thickness for EuIG and up to 90 nm for TbIG) were fully strained to the substrate lattice parameter, with the TbIG film exhibiting in-plane compressive strain on GGG and in-plane tension on SGGG, and the EuIG exhibiting in-plane compression on GGG. The EuIG/GGG (111) and (100) and the TbIG/GGG (111) films exhibit PMA. XRD indicates high crystal quality although the films were deficient in Fe, with RE : Fe = 0.70–0.72, and the excess RE cations are believed to be accommodated in the octahedral sites. For TbIG, the increase in average magnetic moment of the octahedral sites is believed to be responsible for the increase in compensation temperature of the films (~335 K) compared to bulk, measured by magnetometry, Faraday rotation, and SMR.

Pt/(Tb,Eu)IG heterostructure Hall bars showed the existence of AHE-like SMR at the metal/garnet interface. The imaginary part of the spin mixing conductance of these heterostructures was of the same order of magnitude as that of the previously studied Pt/TmIG system, with values ranging from 4.6 to $5.4 \times 10^{12} \, \Omega^{-1} \, \text{m}^{-2}$. Also, G_i was similar between Pt/EuIG (001) and Pt/EuIG (111), in contrast to past work on Pt/CFO. FMR measurements of EuIG (111) were also performed, giving the first measurement of the Gilbert damping parameter in this material. These RE garnets exhibit promise for future spintronic experiments and applications that require ferrimagnetic insulators with PMA for different crystal orientations or with both PMA and a magnetic compensation point.

VI. METHODS

Thin Film Fabrication and Characterization. All thin films were deposited using pulsed laser deposition (PLD) on single-crystal GGG and SGGG substrates. The EuIG and TbIG targets used were fabricated in-house by mixing Eu_2O_3, Tb_4O_7, and Fe_2O_3 powders in the proper weight ratios with a ball mill, calcining the green body at 1150 °C for 5 hours, regrinding the powders, and sintering at 1350 °C for 10 hours. The single-phase iron-garnet nature of the targets was confirmed with x-ray diffraction. The growth conditions used were a substrate backside temperature of 900 °C, a laser fluence of 1.3 J/cm², a laser repetition rate of 10 Hz, and an O_2 pressure of 150 mTorr. After the deposition, the samples were cooled back to room temperature at a rate of 20 °C per minute in 150 mTorr O_2 (slower cooling was not found to be necessary to increase sample quality). AFM RMS roughness measurements were carried out in a Digital Instruments Nanoscope IV with a 1 μm x 1 μm scan size, XRD measurements were carried out in a

Bruker D8 Discover HRXRD, and magnetic measurements were carried out in an ADE 1660 VSM and a Quantum Design MPMS3.

Compositional Characterization. A Thermo Scientific K-Alpha+ system was used to take high-resolution XPS spectra for compositional analysis. Prior to data acquisition, a mild argon cluster cleaning procedure was used to remove adventitious carbon without affecting film stoichiometry. High-resolution data were acquired with a 50-eV pass energy. Data analysis was accomplished by comparing integrated peak areas in AVANTAGE. The ALTHERMO1 relative sensitivity factor database was used to correctly weight the atomic ratios.

Hall Cross Fabrication. Hall crosses of two different sizes (100 μm and 50 μm widths) were fabricated in a two-step lithography process. First, a negative image was defined on a garnet film with a sputtered Pt overlayer and ion milling was used to create mesa structures. Plasma ashing was necessary to remove residual resist after this step. Then, an aligned positive patterning step was used to define areas for Au/Ta gold contacts. The spintronic properties of these Hall crosses were measured in a homemade four-point probe station.

FMR. Broadband FMR measurements were performed using a NanoOsc Phase FMR spectrometer and 200-μm-wide coplanar waveguide. The sample is subjected to a DC magnetic field H along the film plane, in addition to a small time-varying microwave excitation field perpendicular to it. The frequency f varies from 3 to 6 GHz in steps of 0.5 GHz. For each value of f, H is swept from 4500 Oe to 0 Oe in order to saturate the sample and then find the resonance value H_{res} and the linewidth ΔH, by fitting the detected voltage with the derivative of the sum of a symmetric and an antisymmetric Lorentzian:

$$P = \frac{d}{dH}\left[\frac{S\Delta H^2 + A_S(H - H_{\text{res}})}{4(H - H_{\text{res}})^2 + \Delta H^2} \right]. \qquad (7)$$

S and A_S are arbitrary fitting constants. In order to minimize systematic errors arising from miscalibration of Hall sensor the values of H_{res} were averaged with H in opposite directions [60].

ACKNOWLEDGMENTS

[1] Y. Kajiwara, K. Harii, S. Takahashi, J. Ohe, K. Uchida, M. Mizuguchi, H. Umezawa, H. Kawai, K. Ando, K. Takanashi, S. Maekawa, and E. Saitoh, Nature (London) **464**, 262 (2010).

[2] K. Uchida, H. Adachi, T. Ota, H. Nakayama, S. Maekawa, and E. Saitoh, Appl. Phys. Lett. **97**, 172505 (2010).

[3] K. Uchida, H. Adachi, Y. Kajiwara, S. Maekawa, and E. Saitoh, in *Recent Advances in Magnetic Insulators - From Spintronics to Microwave Applications*, edited by M. Wu and A. Hoffmann, 1st ed. (Academic Press, Cambridge, MA, 2013), Vol. 64, pp. 1–27.

[4] P. Li, T. Liu, H. Chang, A. Kalitsov, W. Zhang, G. Csaba, W. Li, D. Richardson, A. DeMann, G. Rimal, H. Dey, J. S. Jiang, W. Porod, S. B. Field, J. Tang, M. C. Marconi, A. Hoffmann, O. Mryasov, and M. Wu, Nat. Commun. **7**, 12688 (2016).

[5] C. O. Avci, A. Quindeau, C.-F. Pai, M. Mann, L. Caretta, A. S. Tang, M. C. Onbasli, C. A. Ross, and G. S. D. Beach, Nat. Mater. **16**, 309 (2017).

[6] D. Apalkov, B. Dieny, and J. M. Slaughter, Proc. IEEE **104**, 1796 (2016).

[7] S.-W. Lee and K.-J. Lee, Proc. IEEE **104**, 1831 (2016).

[8] I. M. Miron, K. Garello, G. Gaudin, P.-J. Zermatten, M. V. Costache, S. Auffret, S. Bandiera, B. Rodmacq, A. Schuhl, and P. Gambardella, Nature (London) **476**, 189 (2011).

[9] L. Liu, C.-F. Pai, Y. Li, H. W. Tseng, D. C. Ralph, and R. A. Buhrman, Science **336**, 555 (2012).

[10] L. Liu, O. J. Lee, T. J. Gudmundsen, D. C. Ralph, and R. A. Buhrman, Phys. Rev. Lett. **109**, 096602 (2012).

[11] K. Garello, C. O. Avci, I. M. Miron, M. Baumgartner, A. Ghosh, S. Auffret, O. Boulle, G. Gaudin, and P. Gambardella, Appl. Phys. Lett. **105**, 212402 (2014).

[12] M. Kubota, K. Shibuya, Y. Tokunaga, F. Kagawa, A. Tsukazaki, Y. Tokura, and M. Kawasaki, J. Magn. Magn. Mater. **339**, 63 (2013).

[13] J. Fu, M. Hua, X. Wen, M. Xue, S. Ding, M. Wang, P. Yu, S. Liu, J. Han, C. Wang, H. Du, Y. Yang, and J. Yang, Appl. Phys. Lett. **110**, 202403 (2017).

[14] H. Wang, C. Du, P. C. Hammel, and F. Yang, Phys. Rev. B **89**, 134404 (2014).

[15] W. Yang, S. Yang, Q. Zhang, Y. Xu, S. Shen, J. Liao, J. Teng, C. Nan, L. Gu, Y. Sun, K. Wu, and Y. Li, Appl. Phys. Lett. **105**, 092411 (2014).

[16] M. Isasa, A. Bedoya-Pinto, S. Vélez, F. Golmar, F. Sánchez, L. E. Hueso, J. Fontcuberta, and F. Casanova, Appl. Phys. Lett. **105**, 142402 (2014).

[17] P. C. Dorsey, P. Lubitz, D. B. Chrisey, and J. S. Horwitz, J. Appl. Phys. **79**, 6338 (1998).

[18] M. Kubota, A. Tsukazaki, F. Kagawa, K. Shibuya, Y. Tokunaga, M. Kawasaki, and Y. Tokura, Appl. Phys. Express **5**, 103002 (2012).

[19] A. Quindeau, C. O. Avci, W. Liu, C. Sun, M. Mann, A. S. Tang, M. C. Onbasli, D. Bono, P. M. Voyles, Y. Xu, J. Robinson, G. S. D. Beach, and C. A. Ross, Adv. Electron. Mater. **3**, 1600376 (2016).

[20] H. Yamahara, M. Mikami, M. Seki, and H. Tabata, J. Magn. Magn. Mater. **323**, 3143 (2011).

[21] N. Kumar, N. G. Kim, Y. A. Park, N. Hur, J. H. Jung, K. J. Han, and K. J. Yee, Thin Solid Films **516**, 7753 (2008).

[22] E. Lage, L. Beran, A. U. Quindeau, L. Ohnoutek, M. Kucera, R. Antos, S. R. Sani, G. F. Dionne, M. Veis, and C. A. Ross, APL Mater. **5**, 036104 (2017).

[23] E. Popova, A. F. Franco Galeano, M. Deb, B. Warot-Fonrose, H. Kachkachi, F. Gendron, F. Ott, B. Berini, and N. Keller, J. Magn. Magn. Mater. **335**, 139 (2013).

[24] P. Sellappan, C. Tang, J. Shi, and J. E. Garay, Mater. Res. Lett. **5**, 41 (2017).

[25] S. Geprägs, A. Kehlberger, F. Della Coletta, Z. Qiu, E.-J. Guo, T. Schulz, C. Mix, S. Meyer, A. Kamra, M. Althammer, H. Huebl, G. Jakob, Y. Ohnuma, H. Adachi, J. Barker, S. Maekawa, G. E. W. Bauer, E. Saitoh, R. Gross, S. T. B. Goennenwein, and M. Kläui, Nat. Commun. **7**, 10452 (2016).

[26] C. L. Jermain, H. Paik, S. V. Aradhya, R. A. Buhrman, D. G. Schlom, and D. C. Ralph, Appl. Phys. Lett. **109**, 192408 (2016).

[27] C. N. Wu, C. C. Tseng, K. Y. Lin, C. K. Cheng, S. L. Yeh, Y. T. Fanchiang, M. Hong, and J. Kwo, AIP Adv. **8**, 055904 (2018).

[28] C. O. Avci, E. Rosenberg, M. Baumgartner, L. Beran, A. Quindeau, P. Gambardella, C. A. Ross, and G. S. D. Beach, Appl. Phys. Lett. **111**, 072406 (2017).

[29] J. Li, G. Yu, C. Tang, Y. Liu, Z. Shi, Y. Liu, A. Navabi, M. Aldosary, Q. Shao, K. L. Wang, R. Lake, and J. Shi, Phys. Rev. B **95**, 241305 (2017).

[30] C. Tang, P. Sellappan, Y. Liu, Y. Xu, J. E. Garay, and J. Shi, Phys. Rev. B **94**, 140403 (2016).

[31] *Landolt-Börnstein - Group III Crystal and Solid State Physics*, edited K.-H. Hellwege and A. M. Hellwege (Springer-Verlag, Berlin/Heidelberg, 1978), Vol. 12a.

[32] S. Iida, J. Phys. Soc. Japan **22**, 1201 (1967).

[33] Y. Sun, Y.-Y. Song, H. Chang, M. Kabatek, M. Jantz, W. Schneider, M. Wu, H. Schultheiss, and A. Hoffmann, Appl. Phys. Lett. **101**, 152405 (2012).

[34] D.-Y. Lu, T. Ogata, H. Unuma, X.-C. Li, N.-N. Li, and X.-Y. Sun, Solid State Ionics **201**, 6 (2011).

[35] D.-Y. Lu, Solid State Ionics **276**, 98 (2015).

[36] M. Balaguer, C.-Y. Yoo, H. J. M. Bouwmeester, and J. M. Serra, J. Mater. Chem. A **1**, 10234 (2013).

[37] E.-J. Cho and S.-J. Oh, Phys. Rev. B **59**, R15613 (1999).

[38] D. H. Kim, N. M. Aimon, L. Bi, J. M. Florez, G. F. Dionne, and C. A. Ross, J. Phys. Condens. Matter **25**, 026002 (2013).

[39] R. O'Handley, *Modern Magnetic Materials: Principles and Applications*, 1st ed. (Wiley, New York, NY, 1999).

[40] B. D. Cullity, *Elements of X-Ray Diffraction*, 2nd ed. (Addison-Wesley Publishing Company, Inc, Reading, MA, 1978).

[41] G. F. Dionne, *Magnetic Oxides*, 1st ed. (Springer Science+Business Media, New York, NY, 2009).

[42] Z. Zhou, Y. Zhang, Z. Wang, W. Wei, W. Tang, J. Shi, and R. Xiong, Appl. Surf. Sci. **254**, 6972 (2008).

[43] T.-C. Lin, G. Seshadri, and J. A. Kelber, Appl. Surf. Sci. **119**, 83 (1997).

[44] T. Taffary, D. Autissier, F. Boust, and H. Pascard, IEEE Trans. Magn. **34**, 1384 (1998).

[45] V. Sharma and B. K. Kuanr, J. Alloys Compd. **748**, 591 (2018).

[46] Y.-T. Chen, S. Takahashi, H. Nakayama, M. Althammer, S. T. B. Goennenwein, E. Saitoh, and G. E. W. Bauer, Phys. Rev. B **87**, 144411 (2013).

[47] M. Weiler, G. Woltersdorf, M. Althammer, H. Huebl, and S. T. B. Goennenwein, in *Solid State Physics* (Academic Press, Cambridge, MA, 2013), pp. 123–156.

[48] B. F. Miao, S. Y. Huang, D. Qu, and C. L. Chien, Phys. Rev. Lett. **112**, 236601 (2014).

[49] M. Althammer, S. Meyer, H. Nakayama, M. Schreier, S. Altmannshofer, M. Weiler, H. Huebl, S. Geprägs, M. Opel, R. Gross, D. Meier, C. Klewe, T. Kuschel, J.-M. Schmalhorst, G. Reiss, L. Shen, A. Gupta, Y.-T. Chen, G. E. W. Bauer, E. Saitoh, and S. T. B. Goennenwein, Phys. Rev. B **87**, 224401 (2013).

[50] S. Geprägs, S. Meyer, S. Altmannshofer, M. Opel, F. Wilhelm, A. Rogalev, R. Gross, and S. T. B. Goennenwein, Appl. Phys. Lett. **101**, 262407 (2012).

[51] Y. M. Lu, Y. Choi, C. M. Ortega, X. M. Cheng, J. W. Cai, S. Y. Huang, L. Sun, and C. L. Chien, Phys. Rev. Lett. **110**, 147207 (2013).

[52] S. Geprägs, S. T. B. Goennenwein, M. Schneider, F. Wilhelm, K. Ollefs, A. Rogalev, M. Opel, and R. Gross, arXiv:1307.4869 (2013).

[53] T. Kuschel, C. Klewe, J.-M. Schmalhorst, F. Bertram, O. Kuschel, T. Schemme, J. Wollschläger, S. Francoual, J. Strempfer, A. Gupta, M. Meinert, G. Götz, D. Meier, and G. Reiss, Phys. Rev. Lett. **115**, 097401 (2015).

[54] C. Onur Avci, E. Rosenberg, J. Mendil, L. Beran, P. Gambardella, C. A. Ross, and G. S. D. Beach (unpublished).

[55] A. B. Cahaya, A. O. Leon, and G. E. W. Bauer, Phys. Rev. B **96**, 144434 (2017).

[56] A. K. Zvezdin and V. A. Kotov, *Modern Magnetooptics and Magnetooptical Materials* (CRC, Boca Raton, FL, 1997).

[57] K. Ganzhorn, J. Barker, R. Schlitz, B. A. Piot, K. Ollefs, F. Guillou, F. Wilhelm, A. Rogalev, M. Opel, M. Althammer, S. Geprägs, H. Huebl, R. Gross, G. E. W. Bauer, and S. T. B. Goennenwein, Phys. Rev. B **94**, 094401 (2016).

[58] J. Finley and L. Liu, Phys. Rev. Appl. **6**, 054001 (2016).

[59] M. Guillot, H. Le Gall, J. M. Desvignes, and M. Artinian, IEEE Trans. Magn. **30**, 4419 (1994).

[60] C. Gonzalez-Fuentes, R. K. Dumas, and C. García, J. Appl. Phys. **123**, 023901 (2018).